



Original Paper

2D Q-compensated multi-component elastic Gaussian beam migration



Chao Chen, Ji-Dong Yang, Xin-Ru Mu, Zhen-Chun Li*, Jian-Ping Huang

China University of Petroleum (East China), Qingdao, 266580, Shandong, China

ARTICLE INFO

Article history:

Received 9 November 2021

Received in revised form

22 June 2022

Accepted 16 September 2022

Available online 21 September 2022

Edited by Jie Hao

Keywords:

Q-compensated

Viscoelastic

Gaussian beam migration

Multi-component

Absorption attenuation

ABSTRACT

Elastic waves are affected by viscoelasticity during the propagation through the Earth, resulting in energy attenuation and phase distortion, in turn resulting in low seismic imaging accuracy. Therefore, viscoelasticity should be considered in seismic migration imaging. We propose a Q compensated multi-component elastic Gaussian beam migration (Q-EGBM) method to (1) separate the elastic-wave data into longitudinal (P) and transverse (S) waves to perform PP-wave and PS-wave imaging; (2) recover the amplitude loss caused by attenuation; (3) correct phase distortions caused by dispersion; (4) improve the resolution of migration imaging. In this paper, to accomplish (2), (3), and (4), we derive complex-valued traveltimes in viscoelastic media. The results of numerical experiments using a simple five-layer model and a sophisticated BP gas model show that the method presented here has significant advantages in recovering energy decay and correcting phase distortion, as well as significantly improving imaging resolution.

© 2023 The Authors. Publishing services by Elsevier B.V. on behalf of KeAi Communications Co. Ltd. This is an open access article under the CC BY-NC-ND license (<http://creativecommons.org/licenses/by-nc-nd/4.0/>).

1. Introduction

During the propagation of seismic waves through the Earth, the influence of viscoelastic media can cause attenuation of seismic wave energy and phase distortion, reducing the resolution of seismic imaging. This can harm the quality of the image and consequently cause difficulties in the interpretation of seismic data.

Hargreaves and Calvert (1991) proposed a Fourier transform-based one-dimensional model inverse Q filtering method for amplitude preserving imaging, but this method does not apply to cases where the Q varies laterally. Mittet et al. (1995) presented a method for including absorption effects in prestack finite-difference migration schemes, which reduces dissipation of seismic energy and diminishes phase distortion. However, the method is in principle unstable since it may support waves with exponential growth in depth. To improve seismic imaging resolution and signal-to-noise ratio, Wang (2006) implemented stable inverse Q filtering, applying stabilization only to the amplitude compensation operator of a full inverse Q-filter (no phase correction). Kirchhoff migration with Q compensation (Traynin

et al., 2008) based on ray theory proved to be capable of calculating frequency-dependent traveltimes and handling moderately complex velocity models. Xie et al. (2009) used a three-dimensional tomographic amplitude inversion approach to estimate the absorption model, which was used in subsequent Q-compensated migration, resulting in mitigated frequency-dependent dissipation effects. For P-wave data, seismic data compensation for frequency-dependent absorption and dispersion is well addressed by the Gaussian beam summation method migration (Bai et al., 2016).

Gaussian beam migration (GBM) is a flexible and efficient migration method that combines computational efficiency with imaging accuracy. It solves caustic problems encountered by Kirchhoff migration, while preserving the dynamics of the wavefield, and is highly adaptable. Popov (1982)'s method for calculating wave fields using Gaussian beams, used to solve the three-dimensional Helmholtz equation point-source problem, enables us to compute those through arbitrary ray caustics without introducing any special functions. After Červený et al. (1982) introduced an asymptotic approach based on Gaussian beam wavefield simulations to calculate transverse wavefields,

* Corresponding author.

E-mail address: leonli@upc.edu.cn (Z.-C. Li).

the use of downward continuation of the Gaussian beam made it possible to solve the wave equations for seismic propagation (Hill and Ross, 1990). The method retains an explanatory ray-path description of this propagation. To describe the efficiency of the Gaussian beam migration calculation and to highlight its advantages, Hale (1992a, 1992b) analyzed the relationship between the Gaussian beam migration and the Kirchhoff migration. Gaussian beam migration of common shot and common receiver data (Nowack et al., 2003) was later investigated to solve the problem of poor sampling of the sources or receivers. Based on previous Gaussian beam migration which only emphasized kinematic imaging capabilities, true amplitude Gaussian beam migration imaging (Gray and Bleistein, 2009) combined a conventional Gaussian beam migration with a true amplitude wave-equation migration. The method uses the Gaussian beam propagation operator as the core of the linearized forward simulation and the migration. Casasanta and Gray (2015) introduced a common-shot (or common-receiver) beam migration implementation, which allows the migration of datasets rich in azimuth, without any regularization pre-processing required. The method solves the problem that sparse acquisition geometries cannot easily meet the requirements for common-offset, common-azimuth (or common-offset-vector) migration. Least-squares Gaussian beam migration (LSGBM) (Hu et al., 2016) provides an optimal estimate of subsurface reflectivity. Yang et al. (2018) performed simultaneous extrapolation of P- and S-mode wavefields using the Kirchhoff-Helmholtz integral solution of the isotropic elastic equations to achieve a common-shot elastic wave Gaussian beam migration. The method can generate clear PP images and avoid the polarity reversal problem in PS images. The least-squares method and the elastic wave Gaussian beam migration method were then combined to present the elastic wave least-squares Gaussian beam migration method (Yue et al., 2019). This method results in crosstalk-attenuated multi-wave images with better subsurface illumination and higher resolution than conventional elastic Gaussian beam migration methods. The present paper extends the previous work to viscoelastic media. We present expressions for complex-valued velocity and complex-valued traveltimes in viscoelastic media. We show how to remove the influence of amplitude attenuation and waveform dispersion by reversing the sign of attenuation- and dispersion-related terms in the complex-valued traveltimes in the Green's function, allowing us to achieve an amplitude-compensated migration. We stabilize the compensation by applying a smooth and maximum-limited gain function (Zhang et al., 2013). We apply this Q-compensation to produce a multi-component elastic Gaussian beam migration algorithm for viscoelastic media using a source-normalized cross-correlation imaging condition.

The rest of this paper is organized as follows: First, based on Gaussian beams and the Green's functions in elastic media, we use the source-normalized cross-correlation imaging condition to derive the imaging equations for elastic media. Then, we obtain the complex-valued traveltimes in viscoelastic media and solve the stability problem. Next, we derive the imaging equations for Gaussian beams in viscoelastic media by combining the effect of viscoelastic media on Gaussian beams with the imaging equations. Finally, we demonstrate the accuracy of the method in this paper using a simple five-layer model and a more complex BP gas model.

2. Methodology

2.1. Elastic Gaussian beam migration

According to Yue (2011), the expressions for P- and S-waves

recorded wavefields $u_m^p(\mathbf{x}; \mathbf{x}_r; \omega)$ and $u_m^s(\mathbf{x}; \mathbf{x}_r; \omega)$ are

$$u_m^p(\mathbf{x}; \mathbf{x}_r; \omega) = -\frac{\Delta L \omega}{4\pi} \sum_{\mathbf{L}} \int \frac{dp_1^p(\mathbf{L})}{p_2^p(\mathbf{L})} \sqrt{\rho(\mathbf{L})} \hat{u}_m^{p*}(\mathbf{x}; \mathbf{L}; \omega) \times [W_1^p(\mathbf{L})D_1^p(L; p_x^p; \omega) + W_2^p(\mathbf{L})D_2^p(L; p_x^p; \omega)] \quad (1)$$

$$u_m^s(\mathbf{x}; \mathbf{x}_r; \omega) = -\frac{\Delta L \omega}{4\pi} \sum_{\mathbf{L}} \int \frac{dp_1^s(\mathbf{L})}{p_2^s(\mathbf{L})} \sqrt{\rho(\mathbf{L})} \hat{u}_m^{s*}(\mathbf{x}; \mathbf{L}; \omega) \times [W_1^s(\mathbf{L})D_1^s(L; p_x^s; \omega) + W_2^s(\mathbf{L})D_2^s(L; p_x^s; \omega)] \quad (2)$$

The expression for the source wavefield is

$$U_m^p(\mathbf{x}; \mathbf{x}_s; \omega) \approx \frac{i}{4\pi v_p^2(\mathbf{x}_s)} \sqrt{\frac{\omega_r w_0^2}{\rho(\mathbf{x}_s)}} \int \frac{dp_1^p(\mathbf{x}_s)}{p_2^p(\mathbf{x}_s)} \hat{u}_m^p(\mathbf{x}; \mathbf{x}_s; \omega) \quad (3)$$

Here: superscripts p and s refer to P-mode and S-mode, \mathbf{x}_s is the source location, \mathbf{x}_r is the receiver location, \mathbf{x} is the image point, \mathbf{L} is the horizontal coordinate of the beam center, ΔL is the beam center spacing, ω is the angular frequency, p_1 and p_2 are the horizontal and vertical components of the slowness vector at the initial position of the Gaussian beam, ρ is the density, \hat{u}_m^{p*} and \hat{u}_m^{s*} are the expressions for P-wave and S-wave Gaussian beams (Červený and Pšenčík 1983a; Červený and Pšenčík, 1983b; 1984), v_p is P-wave velocity, w_0 is the initial beam width of the Gaussian beam, which can be obtained from Hill and Ross (1990, 2001), ω_r is the reference frequency (Hill and Ross, 1990, 2001), i is an imaginary unit, $D_n^v(L; p_x^v; \omega)$ (Xu et al., 2014) is a windowed local tilt superimposition of multi-component seismic records of different waveforms:

$$D_n^v(L; P_1^v; \omega) = \sqrt{\frac{|\omega|}{2\pi}} \int_S dx_r u_n(\mathbf{x}_r; \omega) \exp \left[i\omega p_1^v(\mathbf{L})(x_r - L) - \frac{|\omega|}{\omega_r} \left| \frac{(x_r - L)^2}{2w_0^2} \right| \right] \quad (4)$$

Here, weight coefficients $W_1^v(\mathbf{L})$, $W_2^v(\mathbf{L})$ (Xu et al., 2014) are

$$W_1^p(\mathbf{L}) = 2\gamma^2(\mathbf{L})p_2^p(\mathbf{L})e_1^p(\mathbf{L}), W_2^p(\mathbf{L}) = 2\gamma^2(\mathbf{L})p_2^p(\mathbf{L})e_2^p(\mathbf{L}) + \left(\frac{1 - 2\gamma^2(\mathbf{L})}{v_p(\mathbf{L})} \right) \quad (5)$$

$$W_1^s(\mathbf{L}) = p_2^s(\mathbf{L})e_1^s(\mathbf{L}) + p_1^s(\mathbf{L})e_2^s(\mathbf{L}), W_2^s(\mathbf{L}) = -2p_1^s(\mathbf{L})e_1^s(\mathbf{L}), \gamma(\mathbf{L}) = \frac{v_s(\mathbf{L})}{v_p(\mathbf{L})} \quad (6)$$

Then, we use the source-normalized cross-correlation imaging condition (Claerbout, 1971; Kaelin and Guitton, 2006), which is equivalent to the deconvolution imaging condition using a matched filter in the frequency domain (Lee et al., 1991). This imaging condition is different from the modified dot-product imaging condition of Yang et al. (2018). Yang et al. (2018)'s imaging condition does not need polarity correction while the imaging condition here is more conducive to the comparison of imaging results, which is more convincing. The equations for PP wave and PS wave imaging are

$$I^{PP}(\mathbf{x}) = \int \frac{U_2^{p*}(\mathbf{x}, \mathbf{x}_s, \omega) U_1^p(\mathbf{x}, \mathbf{x}_r, \omega)}{U_2^{p*}(\mathbf{x}, \mathbf{x}_s, \omega) U_2^p(\mathbf{x}, \mathbf{x}_s, \omega)} d\omega$$

$$= \frac{\Delta L}{\sqrt{\omega_r W_0^2}} \sqrt{\rho(\mathbf{L}) \rho(\mathbf{x}_s)} \sum_L \int i \omega v_p^2(\mathbf{x}_s) d\omega \int \frac{dp_1^p(\mathbf{L}) p_2^p(\mathbf{x}_s)}{p_2^p(\mathbf{L}) dp_1^p(\mathbf{x}_s)} \quad (7)$$

$$\times \frac{\hat{u}_1^{p*}(\mathbf{x}; \mathbf{L}; \omega)}{\hat{u}_2^p(\mathbf{x}; \mathbf{x}_s; \omega)} [W_1^p(\mathbf{L}) D_1^p(L; p_1^p; \omega) + W_2^p(\mathbf{L}) D_2^p(L; p_1^p; \omega)]$$

$$I^{PS}(\mathbf{x}) = \int \frac{U_2^{p*}(\mathbf{x}, \mathbf{x}_s, \omega) U_1^s(\mathbf{x}, \mathbf{x}_r, \omega)}{U_2^{p*}(\mathbf{x}, \mathbf{x}_s, \omega) U_2^p(\mathbf{x}, \mathbf{x}_s, \omega)} d\omega$$

$$= \frac{\Delta L}{\sqrt{\omega_r W_0^2}} \sqrt{\rho(\mathbf{L}) \rho(\mathbf{x}_s)} \sum_L \int i \omega v_p^2(\mathbf{x}_s) d\omega \int \frac{dp_1^s(\mathbf{L}) p_2^p(\mathbf{x}_s)}{p_2^s(\mathbf{L}) dp_1^p(\mathbf{x}_s)}$$

$$\times \frac{\hat{u}_1^s(\mathbf{x}; \mathbf{L}; \omega)}{\hat{u}_2^p(\mathbf{x}; \mathbf{x}_s; \omega)} [W_1^s(\mathbf{L}) D_1^s(L; p_1^s; \omega) + W_2^s(\mathbf{L}) D_2^s(L; p_1^s; \omega)] \quad (8)$$

When imaging the converted wave, the converted wave P–S imaging can show a polarity reversal in the migration profile due to different polarization directions. Fig. 1 shows the formation of the P–S converted wave (Du et al., 2012). α is the incidence angle of the P-wave relative to migration dip. In Fig. 1, in the case that positive directions are counterclockwise and right, when the incident P-wave reaches O_1 and O_2 , because $\alpha_1 < 0$ and $\alpha_2 > 0$, the P–S converted wave generated at point O_1 has a negative horizontal displacement component and the P–S converted wave generated at point O_2 has a positive horizontal displacement component, in turn causing the horizontal component seismic recordings received at points R_1 and R_2 to have opposite polarities. Therefore, we correct the imaging results according to the positive or negative angle of incidence α of the P-wave. A sign function $\text{sgn}(\alpha)$ is introduced to correct the sign of the incident angle of the P-wave, and the polarity-corrected P–S imaging equation takes the following form:

$$I^{PS}(\mathbf{x}) = \frac{\Delta L}{\sqrt{\omega_r W_0^2}} \sqrt{\rho(\mathbf{L}) \rho(\mathbf{x}_s)} \sum_L \int i \omega v_p^2(\mathbf{x}_s) d\omega \int \frac{dp_1^s(\mathbf{L}) p_2^p(\mathbf{x}_s)}{p_2^s(\mathbf{L}) dp_1^p(\mathbf{x}_s)} \text{sgn}(\alpha)$$

$$\times \frac{\hat{u}_1^s(\mathbf{x}; \mathbf{L}; \omega)}{\hat{u}_2^p(\mathbf{x}; \mathbf{x}_s; \omega)} [W_1^s(\mathbf{L}) D_1^s(L; p_1^s; \omega) + W_2^s(\mathbf{L}) D_2^s(L; p_1^s; \omega)] \quad (9)$$

2.2. Viscoelastic Gaussian beam migration

Within the frequency band of seismic exploration, the quality factor Q , which characterizes the strength of the viscosity, can be seen as frequency independent, i.e., the constant Q model can be used. In this way, the propagation of the acoustic wave in viscoacoustic media can be seen as it propagates with a complex velocity in acoustic media. In weakly viscous media ($\frac{1}{Q} \ll 1$), the complex velocity can be expressed as (Aki and Richards, 2002)

$$v(\mathbf{x}, \omega) = v_0(\mathbf{x}) \left[1 + \frac{i}{2} Q^{-1}(\mathbf{x}) + \frac{1}{\pi} Q^{-1}(\mathbf{x}) \ln(\omega/\omega_r) \right] \quad (10)$$

Here: $v(\mathbf{x}, \omega)$ is the complex velocity in viscoacoustic media, $v_0(\mathbf{x})$ is the velocity in acoustic media, Q is a quality factor, In Eq. (10), the dispersion reference frequency ω_r is arbitrary, best chosen to be near the geometric mean of the low and high frequencies present in

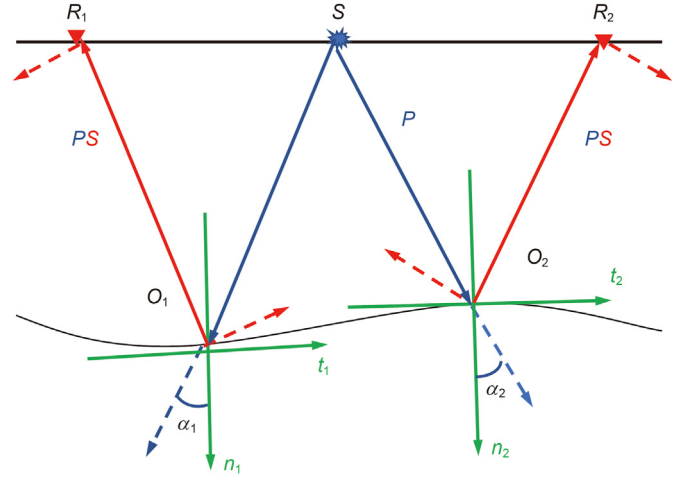


Fig. 1. The formation of the P–S converted wave.

the data. Here, we choose ω_r to be the same as the Gaussian beam reference frequency. In viscous media, Eq. (10) expresses an inherent dispersion relation, and the exponential attenuation of the energy of an elastic wave as it travels along the ray is due to the imaginary part of the complex velocity. The dispersion term in the real part of the complex velocity, on the other hand, ensures the accuracy of the solution to the wave equation. Q does not affect the ray path; it only affects the waveform by changing the complex-valued traveltime (Halliwell, 1991; Henk et al., 2001).

Similarly, the propagation of the elastic wave in viscoelastic media can be seen as it propagates with a complex velocity in elastic media. The expressions for the complex velocity of P- and S-waves are

$$\begin{cases} V_P(\mathbf{x}, \omega) = V_{P_0} \left[1 + \frac{i}{2} Q_P^{-1}(\mathbf{x}) + \frac{1}{\pi} Q_P^{-1}(\mathbf{x}) \ln(\omega/\omega_r) \right] \\ V_S(\mathbf{x}, \omega) = V_{S_0} \left[1 + \frac{i}{2} Q_S^{-1}(\mathbf{x}) + \frac{1}{\pi} Q_S^{-1}(\mathbf{x}) \ln(\omega/\omega_r) \right] \end{cases} \quad (11)$$

Here: $V_P(\mathbf{x}, \omega)$ and $V_S(\mathbf{x}, \omega)$ are complex velocities in viscoelastic media, V_{P_0} and V_{S_0} are velocities in elastic media, Q_P and Q_S are quality factors.

The full expressions for complex-valued traveltimes $T_P(\mathbf{x}, \omega)$ and $T_S(\mathbf{x}, \omega)$ can be obtained from the complex velocity:

$$\begin{cases} T_P(\mathbf{x}, \omega) = T_{P_0}(\mathbf{x}) - \frac{i}{2} T'_P(\mathbf{x}) - \frac{1}{\pi} T''_P(\mathbf{x}) \ln(\omega/\omega_r) \\ T_S(\mathbf{x}, \omega) = T_{S_0}(\mathbf{x}) - \frac{i}{2} T'_S(\mathbf{x}) - \frac{1}{\pi} T''_S(\mathbf{x}) \ln(\omega/\omega_r) \end{cases} \quad (12)$$

Here,

$$\begin{cases} T'_P(\mathbf{x}) = \int_{ray} \frac{1}{V_P Q_P} ds \\ T'_S(\mathbf{x}) = \int_{ray} \frac{1}{V_S Q_S} ds \end{cases} \quad (13)$$

Here: $T_{P_0}(\mathbf{x})$ and $T_{S_0}(\mathbf{x})$ are complex-valued times in elastic media, $T'_P(\mathbf{x})$ and $T'_S(\mathbf{x})$ are real-valued factors that provide attenuation and dispersion effects. During forward propagation, the second terms on the RHS of Eq. (12) produce exponential amplitude decay along a ray as it propagates forward in time; reversing the sign of these terms will compensate for the amplitude decay by applying an exponential gain. The third terms on the RHS of Eq. (12)

produce a phase shift (stretch) of the propagating wavelet; this is the effect of dispersion, and its effect is also compensated (squeeze) by reversing the sign of these terms. For the downward continuation of the recorded wavefield, time-reversal (negating the first terms of Eq. (12)) is also needed. So, for the recorded wavefields, reversing the signs of all terms on the RHS of Eq. (12) for either $T_p(\mathbf{x}, \omega)$ (P–P migration) or $T_s(\mathbf{x}, \omega)$ (P–S migration) accomplishes Q-compensated downward continuation. However, the P-wave source wavefield propagates forward in time, so the first term on the RHS of Eq. (12) for $T_p(\mathbf{x}, \omega)$ should not be negated for its downward continuation. But the source wavefield undergoes attenuation and dispersion, which need to be compensated. This compensation is accomplished by reversing the signs of the second and third terms on the RHS of Eq. (12). Therefore, the net effect of Q-compensation for the final migration formula is the application of amplitude and phase compensations along the entire source to receiver raypath. This fully accomplishes Q-compensation; no extra Q-dependence for source normalizations applied in the cross-correlation imaging condition should be applied.

Fig. 2 illustrates the forward modeling and migration in elastic and viscoelastic media. In Fig. 2, $T_{L_s}^p$, $T_{L_r}^s$ and $T_{L_r}^p$ are complex-valued times in elastic media, $T_{L_s}^{p'}$, $T_{L_r}^{s'}$ and $T_{L_r}^{p'}$ are the second and third terms on the RHS of Eq. (12), L_s and L_r indicate the distances along raypaths from the image point to the source and the detection point, respectively.

To stabilize the amplitude compensation, we take P-wave as an example to solve the problem of stability. $-\frac{1}{2}T_p'(\mathbf{x})$ and $-\frac{1}{\pi}T_p'(\mathbf{x})\ln(\omega/\omega_r)$ of Eq. (12) represent the energy absorption and phase shift, respectively. Viscosity affects the waveform through a frequency-dependent dissipation function (Henk et al., 2001):

$$D(\mathbf{x}) = \exp\left[\frac{\omega}{2}T_p'(\mathbf{x})\right] \exp\left[-\frac{i\omega_r}{\pi}T_p'(\mathbf{x})\ln(\omega/\omega_r)\right] \quad (14)$$

where $\exp\left[\frac{\omega}{2}T_p'(\mathbf{x})\right]$ is energy compensation factor. To eliminate the

stability problem, we apply a smooth and maximum-limited gain function proposed by Zhang et al. (2013) to replace the energy compensation factor with a gain function $\varphi(\eta)$:

$$\varphi(\eta) = \begin{cases} \exp(\eta), & \eta \leq \ln(G), \\ G\left[1 - \ln G - 2.5(\ln G)^2\right] \\ + G(1 + 5 \ln G)\eta - 2.5G\eta^2, & \ln(G) < \eta \leq \ln(G) + 0.2, \\ 1.1G, & \eta > \ln(G) + 0.2 \end{cases} \quad (15)$$

where $\eta = \frac{\omega}{2}T_p'(\mathbf{x})$, and G is a predefined gain limit. When η increases, the $\varphi(\eta)$ will not increase infinitely, but will be close to a constant, i.e., the $\varphi(\eta)$ follows the exponential gain of Eq. (14) until it approaches a predefined maximum gain, then smoothly transitions to the maximum gain.

The P- and S-waves fields can be compensated by reversing the signs of the second and third terms on the RHS of Eq. (12). In the case of migration, we obtain the multi-component elastic Gaussian beam migration imaging method for viscoelastic media by replacing the traveltimes of the elastic wave Gaussian beam with this complex-valued traveltimes and reversing the sign of this term.

3. Numerical examples

3.1. Simple five-layer model

First, we use a simple five-layer model, which has 301×201 grid points with a horizontal grid spacing of 10 m and vertical grid spacing of 10 m to evaluate this method. There is a high-attenuation gas-bearing wedge in the third layer. Fig. 3 displays the model parameters, including P-wave velocity Fig. 3a, S-wave velocity Fig. 3b, P-wave quality factor Fig. 3c, and S-wave quality factor Fig. 3d. An explosive P-wave source with a 25 Hz Ricker wavelet is excited at the free surface. The shot spacing is 50 m, and each shot has 301 receivers with 10 m receiver spacing. The sampling time is 3 s with a 1 ms time interval. For the forward simulation, we use the

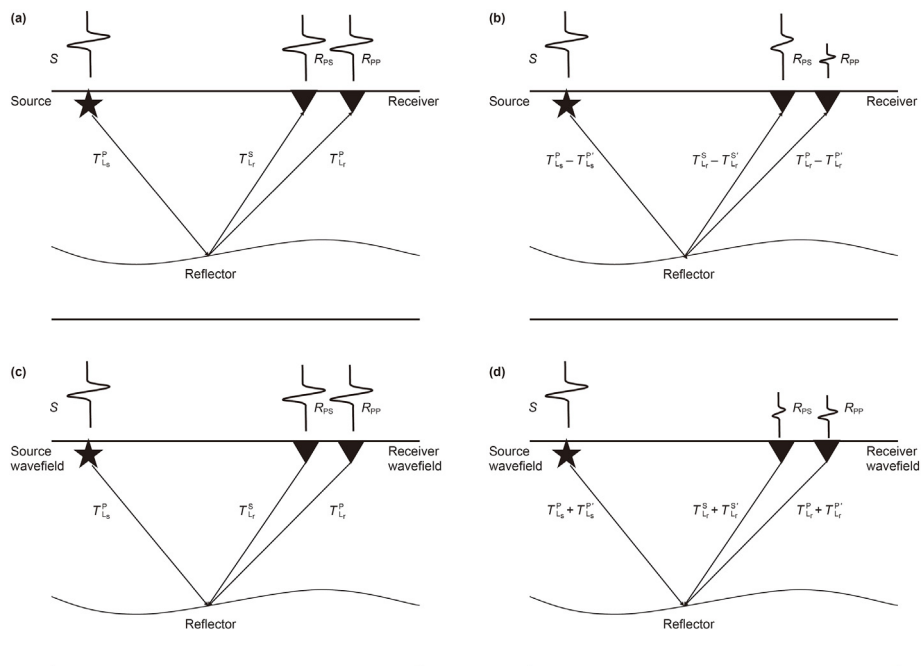


Fig. 2. The forward modeling and migration in elastic and viscoelastic media. (a) forward modeling and (c) migration in elastic media; (b) forward modeling and (d) migration in viscoelastic media.

elastic and viscoelastic high-order staggered grid FD methods (Mu et al. 2021a, 2021b) to generate 60 shot gathers. The modeled horizontal x - and vertical z -component data of the 30th shot at $x_s = 1460$ m are shown in Fig. 4a–d, respectively. Fig. 5a and b shows single trace comparisons selected from Fig. 4 of the x -component and z -component. We can see that the energy of the viscoelastic forward modeling is significantly lower than that of the elastic wave forward modeling, showing how the viscosity absorbs and attenuates the seismic wave during propagation. Elastic wave Gaussian beam migrated image for elastic data (reference image), elastic wave Gaussian beam migrated image (non-compensated) for viscoelastic data and viscoelastic Gaussian beam migrated image (compensated) are exhibited in Fig. 6.

Compared with the reference images in Fig. 6a and d, non-compensated images in Fig. 6b and e exhibit weaker reflective event energy, especially the layers beneath the high-attenuation gas-bearing wedge. We can also see that the compensated images in Fig. 6c and f are close to the reference images, with overall properly recovered amplitudes, e.g., PP and PS-images carry similar amplitude and phase information to those of the references. A more detailed comparison was made by extracting single traces from Fig. 6. Fig. 7 shows the single trace comparison extracted from PP and PS images. Here, the compensated trace (the blue line) is closer to the reference trace (the red line) than the uncompensated trace (the green line), which has a smaller amplitude, and its attenuated amplitude and distorted phase are restored acceptable.

3.2. BP gas model

Next, a more complicated BP gas model (Yang and Zhu, 2019) with a high-attenuation chimney is considered to further test our algorithm. The P- and S-wave velocity models, and P- and S-wave Q models are shown in Fig. 8. All the models have 451×226 grid points with a grid spacing of 10 m in the x -direction and 10 m in the

z -direction. A Ricker wavelet with a 15 Hz dominant frequency is excited as the source wavelet. There are 90 shots with a 50 m spacing interval and 451 receivers with a spacing of 100 m. The sampling time is 3 s with a 0.8 ms time interval. Elastic and viscoelastic high-order staggered grid FD methods for forward simulation are employed to generate the gathers.

Fig. 9 shows the elastic wave Gaussian beam migrated image for elastic data (reference), elastic wave Gaussian beam migrated image (non-compensated for viscoelastic data), and viscoelastic Gaussian beam migrated image (compensated). As can be seen from the area in the blue box, the images below the attenuating chimney in Fig. 9b and e are blurred, and the energy is weak, while the images below the chimney in Fig. 9c and f are significantly improved, and the energy is better recovered. Compared to the uncompensated image, which is indistinct, the bulges on the sides above the anticlinal structure indicated by the arrows in the compensated image are more clearly visible and almost match the reference image. In addition, we also get ADCIGs at the horizontal location of 1000 m. As can be seen from Fig. 10, the event axis are basically flat. Compared with the compensated ADCIG, the deep energy of the uncompensated ADCIG is weaker. The comparison of ADCIGs shows the accuracy of the method in this paper.

Single migrated traces at the horizontal location of 2550 m are selected from Fig. 9 for the more detailed comparison. As shown in Fig. 11, the compensated single trace matches the reference trace, while the uncompensated trace has a significant amplitude loss. Fig. 12 exhibits the average wave number spectra corresponding to the images of Fig. 9, from which it can be seen that the compensated image (blue line) has a higher resolution than the uncompensated image (green line), almost approaching the reference image resolution (red line). In conclusion, the method in this paper overcomes the negative impact of viscoelasticity on image quality and improves image quality and resolution.

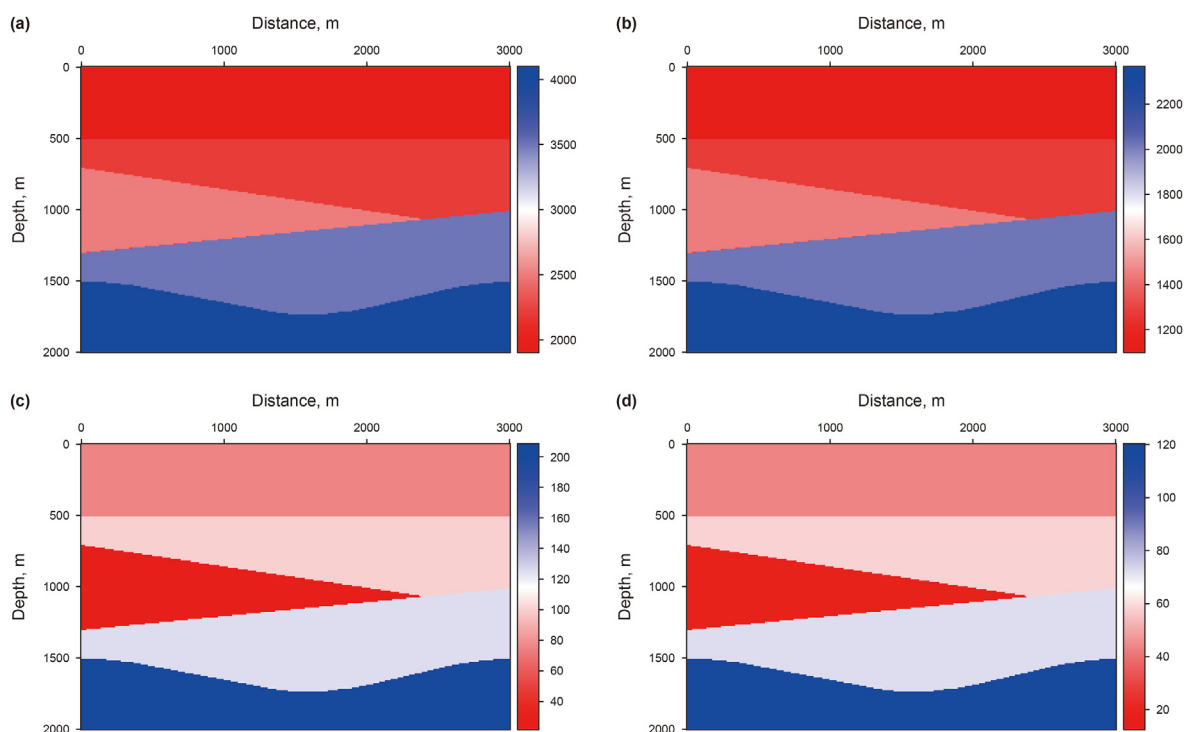


Fig. 3. Simple five-layer models. (a) P-wave velocity model; (b) S-wave velocity model; (c) P-wave Q model; (d) S-wave Q model.

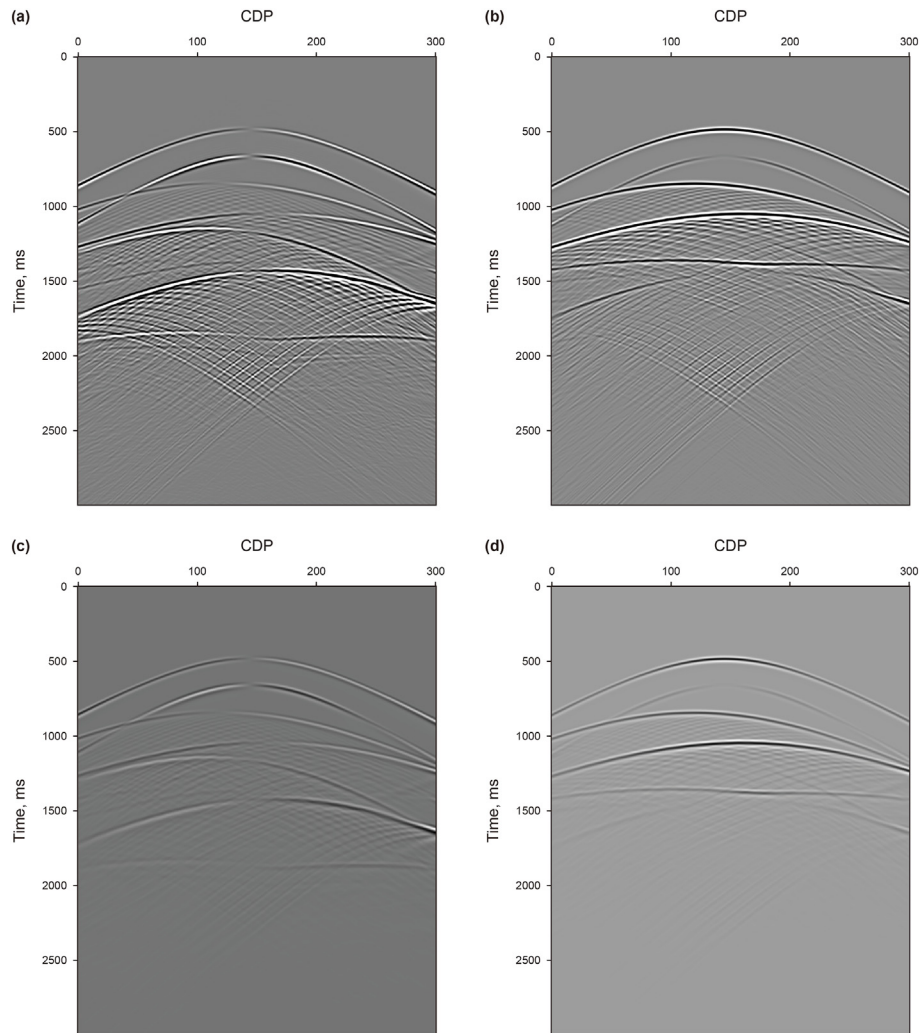


Fig. 4. 30th shot gathers at $x_s = 1460$ m using elastic and viscoelastic modeling methods. (a) elastic FD-modeled x-component; (b) elastic FD-modeled z-component; (c) viscoelastic FD-modeled x-component; (d) viscoelastic FD-modeled z-component.

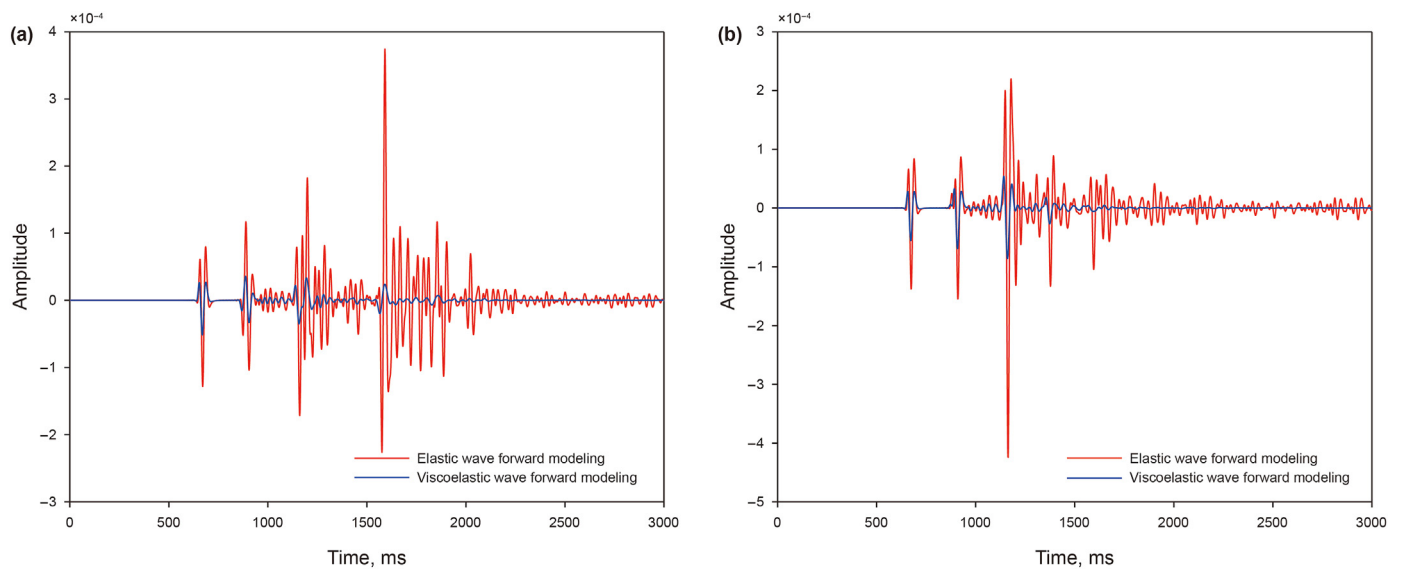


Fig. 5. Single trace comparisons. (a) x-component; (b) z-component.

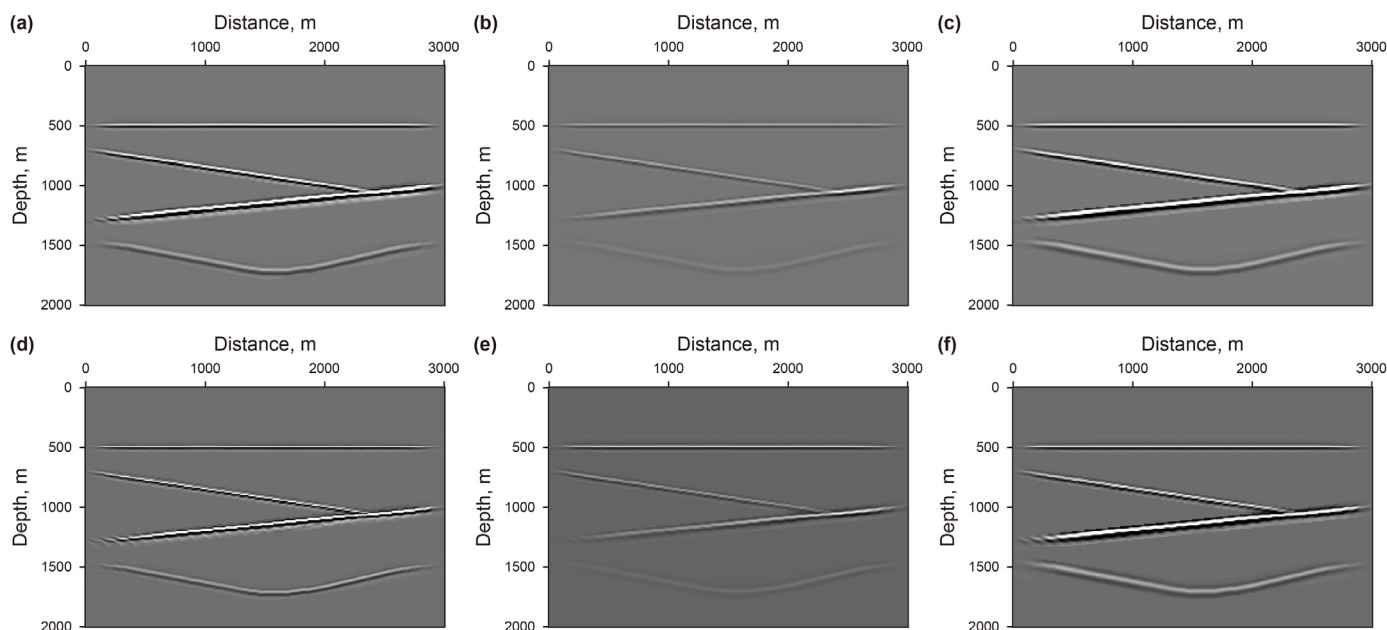


Fig. 6. The migrated images. PP-images. (a) reference EGBM using elastic data; (b) EGBM using viscoelastic data; (c) Q-EGBM using viscoelastic data. PS-images. (d) reference EGBM using elastic data; (e) EGBM using viscoelastic data; (f) Q-EGBM using viscoelastic data.

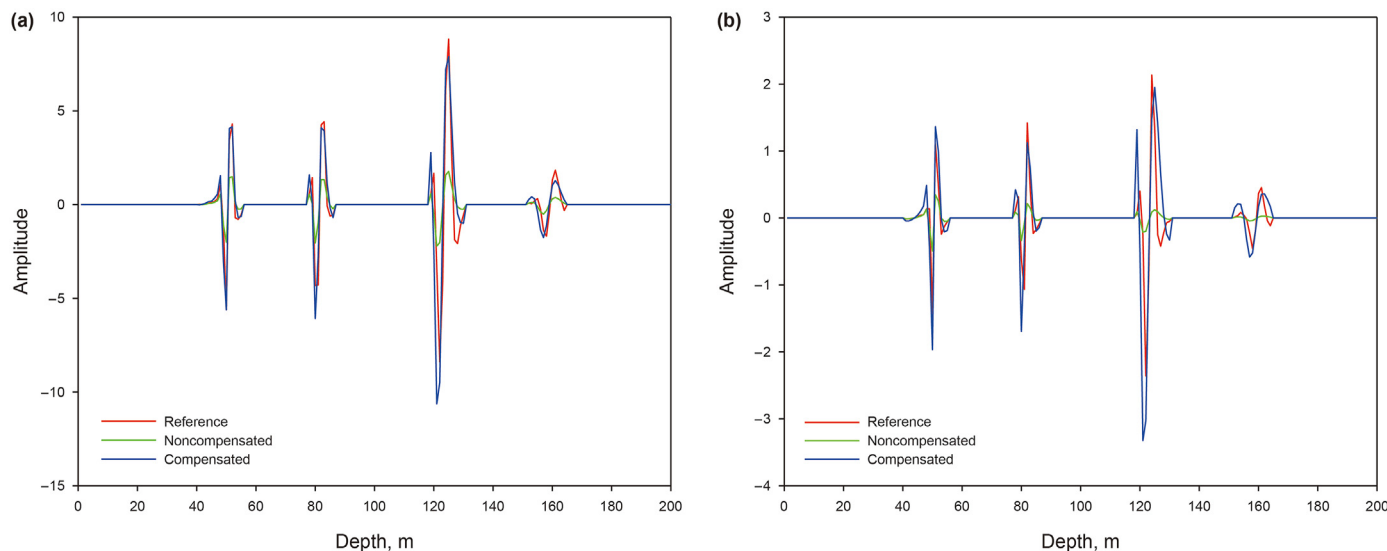


Fig. 7. Single trace comparisons at horizontal locations of 750 m. (a) PP-image; (b) PS-image.

4. Discussion

The presence of viscosity causes energy attenuation and phase distortion during the propagation of seismic waves, causing great difficulties in seismic interpretation. The inverse Q filtering method was first proposed to address the effects of viscosity, but it does not consider both lateral and vertical variations in Q and cannot accurately image complex structures (Bickel and Natarajan 1985; Hargreaves and Calvert, 1991; Wang, 2002). The attenuation compensation method based on ray theory, which only considers the kinematic characteristics of seismic waves, is less satisfactory for imaging complicated media (Zhang and Wapenaar, 2002; Traynin et al., 2008; Xie et al., 2009; Zhang et al., 2013). Attenuation compensation methods based on wave equations enable better

imaging of the subsurface media but are less computationally efficient than laterally invariant methods (Mittet et al., 1995; Mittet, 2007; Valenciano et al., 2011; Wang et al., 2012). The multi-component elastic Gaussian beam migration method based on attenuation compensation in this paper has a more accurate imaging accuracy. The method has three key points: First, based on the elastic Gaussian beams and the corresponding Green's functions, the imaging equations are obtained according to the source-normalized cross-correlation imaging condition that is more conducive to the comparison of imaging results. Second, based on the complex velocity of the Gaussian beam during propagation in viscoelastic media, the complex-valued traveltimes affecting the propagation waveform of the Gaussian beam were presented. Finally, the multi-component elastic Gaussian beam imaging

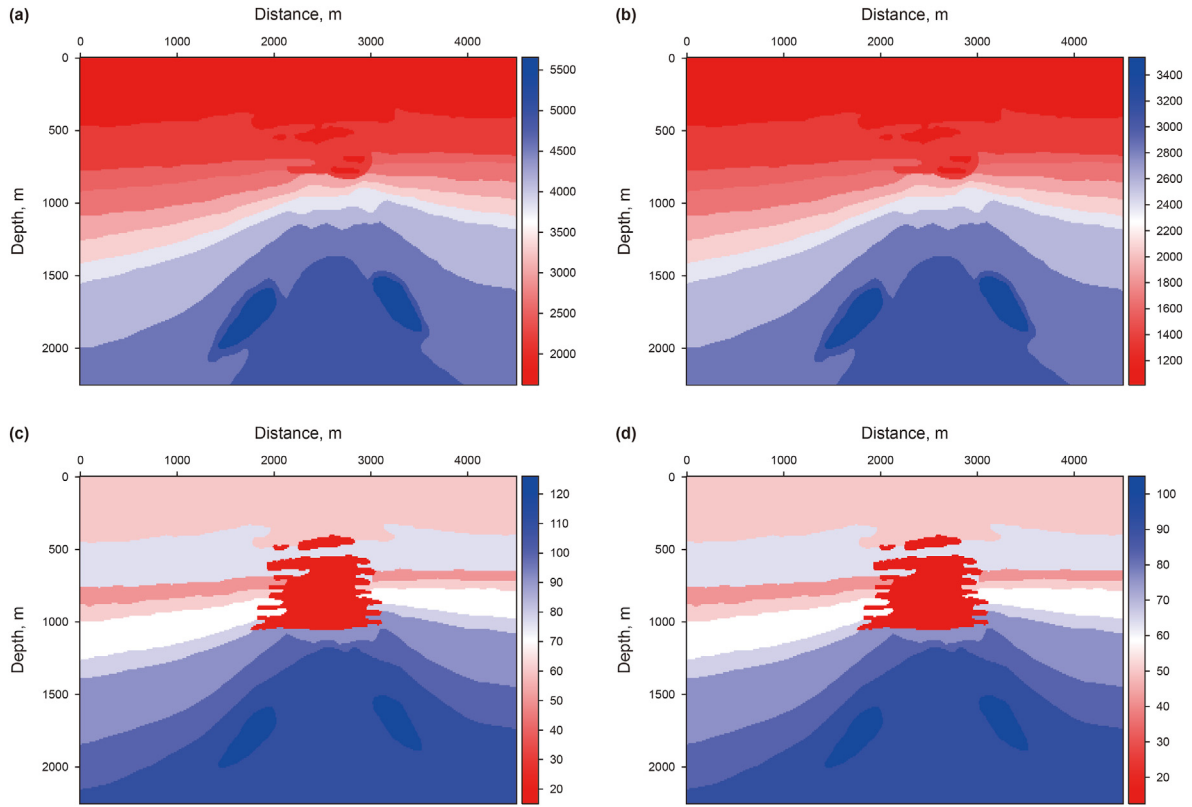


Fig. 8. Complicated BP gas models. (a) P-wave velocity model; (b) S-wave velocity model; (c) P-wave Q model; (d) S-wave Q model.

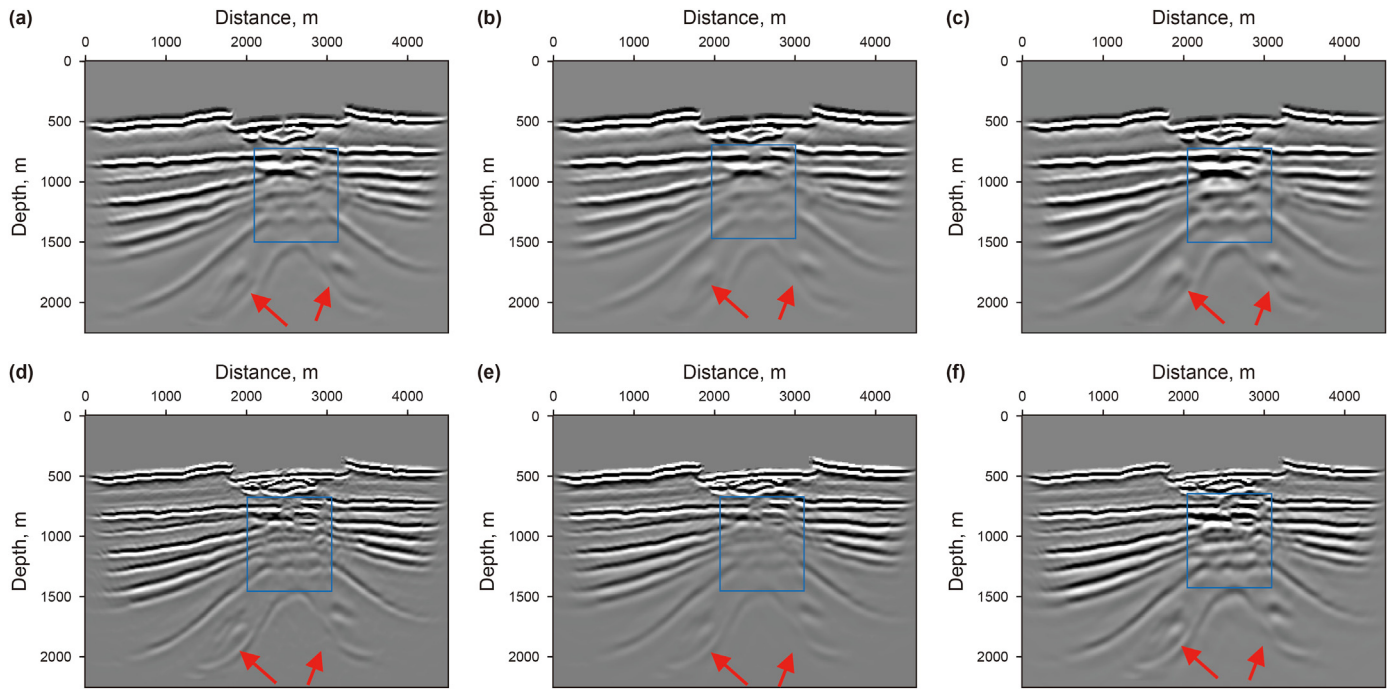


Fig. 9. The migrated images. PP-images. (a) reference EGBM using elastic data; (b) EGBM using viscoelastic data; (c) Q-EGBM using viscoelastic data. PS-images. (d) reference EGBM using elastic data; (e) EGBM using viscoelastic data; (f) Q-EGBM using viscoelastic data.

equations in viscoelastic media were obtained by replacing the Gaussian beam traveltimes with the complex-valued traveltimes in viscoelastic media. Using two models for testing, we showed that

the method presented here not only compensates for absorption attenuation, but also improves resolution. However, compared to the imaging accuracy of the method in this paper, it needs to

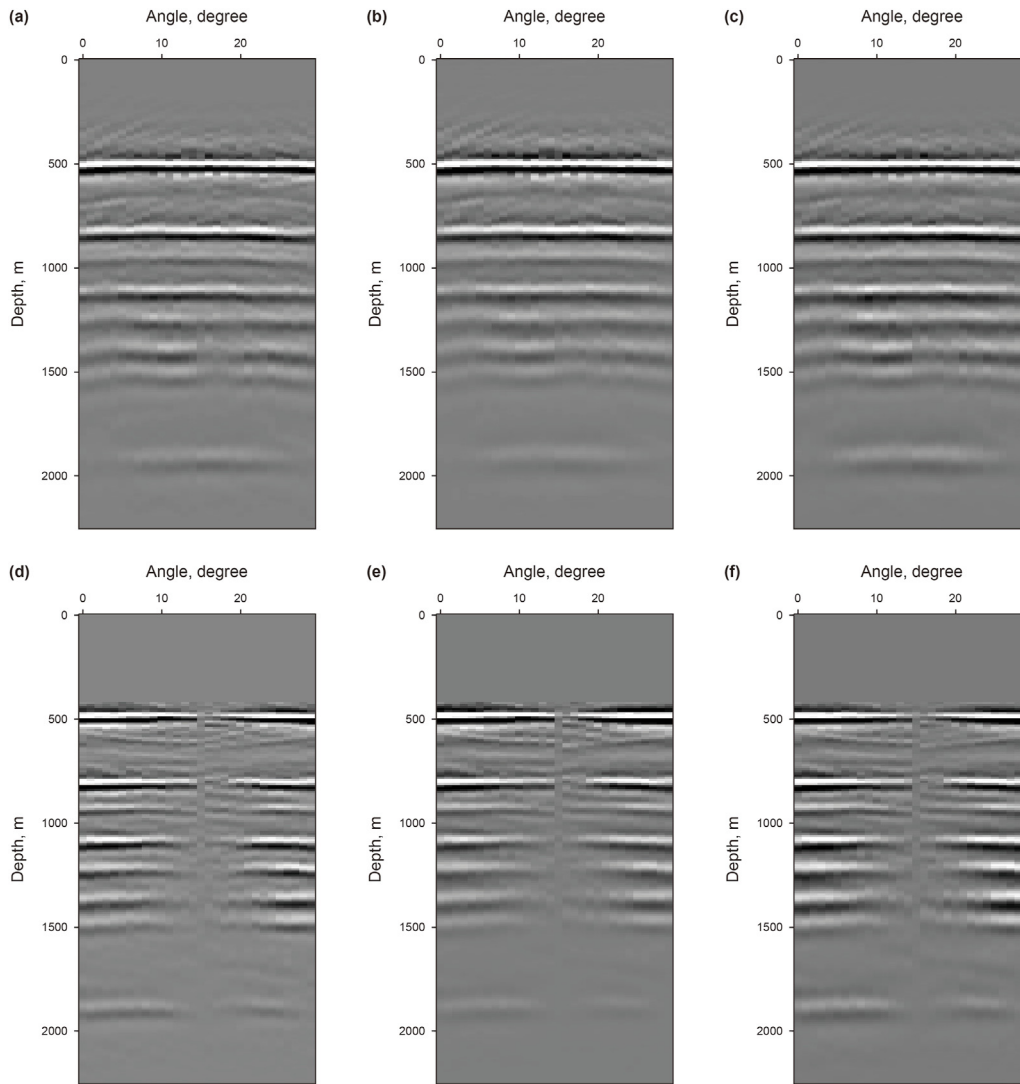


Fig. 10. PP-ADCIGs at the horizontal location of 1000 m. (a) reference EGBM using elastic data; (b) EGBM using viscoelastic data; (c) Q-EGBM using viscoelastic data. PS-ADCIGs at the horizontal location of 1000 m. (d) reference EGBM using elastic data; (e) EGBM using viscoelastic data; (f) Q-EGBM using viscoelastic data.

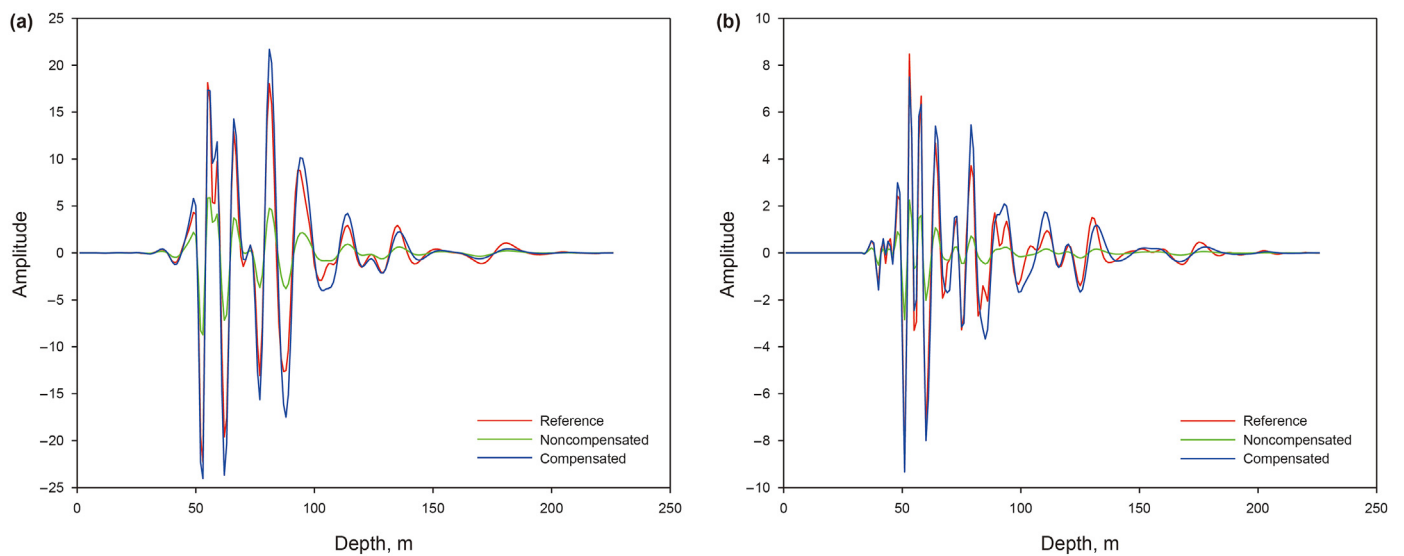


Fig. 11. Single trace comparisons at the horizontal locations of 2550 m (a) PP-image; (b) PS-image.

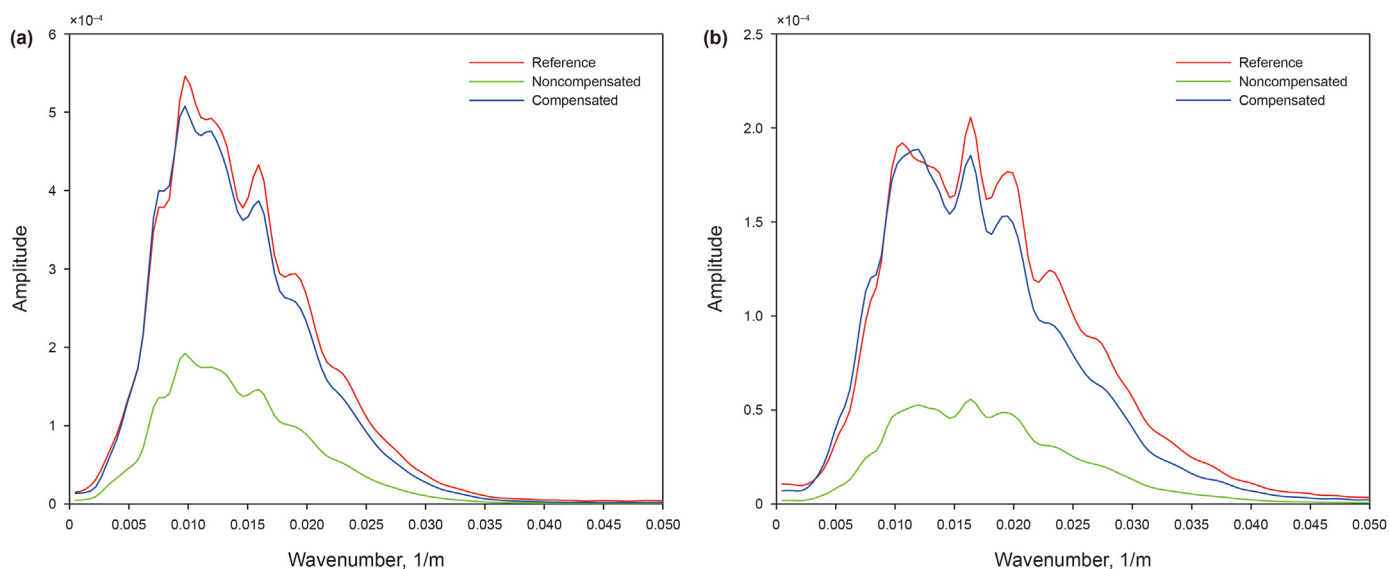


Fig. 12. Average wavenumber spectra shown in Fig. 9. (a) PP-image; (b) PS-image.

consider computational efficiency. Meanwhile, perhaps we should consider using a viscoacoustic deblurring filter (Aoki and Schuster, 2009; Chen et al., 2017) to solve the stabilization problem.

5. Conclusion

We propose a multi-component elastic Gaussian beam migration method applicable to viscoelastic media for amplitude attenuation and phase distortion of seismic wave propagation in viscoelastic media. Compared to conventional acoustic migration methods, the method in this paper considers the vectorial characteristics of the waves and makes additional use of S-waves, which are more sensitive to fluids. Numerical examples show that the method can recover the energy of seismic wave propagation, while improving the resolution of imaging in viscoelastic media.

References

- Aki, K., Richards, P.G., 2002. *Quantitative seismology: Theory and Methods*. University Science Books.
- Aoki, N., Schuster, G.T., 2009. Fast least-squares migration with a deblurring filter. *Geophysics* 74, WCA83–WCA93. <https://doi.org/10.1190/1.3155162>.
- Bai, M., Chen, X.H., Wu, J., et al., 2016. Q-compensated migration by Gaussian beam summation method. *J. Geophys. Eng.* 13, 35–48. <https://doi.org/10.1088/1742-2132/13/1/35>.
- Bickel, S.H., Natarajan, R.R., 1985. Plane-wave Q deconvolution. *Geophysics* 50, 1426–1439. <https://doi.org/10.1190/1.1442011>.
- Casasanta, L., Gray, S.H., 2015. Converted-wave beam migration with sparse sources or receivers. *Geophys. Prospect.* 63. <https://doi.org/10.1111/1365-2478.12226>.
- Červený, V., Pšenčík, I., 1983a. Gaussian beams and paraxial ray approximation in three-dimensional elastic inhomogeneous media. *J. Geophys.* 53, 1–15.
- Červený, V., Pšenčík, I., 1983b. Gaussian beams in two-dimensional elastic inhomogeneous media. *Geophys. J. Int.* 72, 417–433. <https://doi.org/10.1111/j.1365-246X.1983.tb03793.x>.
- Červený, V., Pšenčík, I., 1984. Gaussian beams in elastic 2-D laterally varying layered structures. *Geophys. J. Int.* 78, 65–91. <https://doi.org/10.1111/j.1365-246X.1984.tb06472.x>.
- Červený, V., Popov, M.M., Pšenčík, I., 1982. Computation of wave fields in inhomogeneous media—Gaussian beam approach. *Geophys. J. Int.* 70, 109–128. <https://doi.org/10.1111/j.1365-246X.1982.tb06394.x>.
- Chen, Y.Q., Dutta, G., Dai, W., et al., 2017. Q-least-squares reverse time migration with viscoacoustic deblurring filters. *Geophysics* 82, S425–S438. <https://doi.org/10.1190/segam2017-17640582.1>.
- Claerbout, J.F., 1971. Toward a unified theory of reflector mapping. *Geophysics* 36, 467. <https://doi.org/10.1190/1.1440185>.
- Du, Q.Z., Zhu, Y.T., Ba, J., 2012. Polarity reversal correction for elastic reverse time migration. *Geophysics* 77, 31. <https://doi.org/10.1190/geo2011-0348.1>.
- Gray, S.H., Bleistein, N., 2009. True-amplitude Gaussian-beam migration. *Geophysics* 74, S11–S23. <https://doi.org/10.1190/1.3052116>.
- Hale, D., 1992a. Migration by the Kirchhoff, Slant Stack, and Gaussian Beam Methods. Colorado School of Mines, Golden, CO. <https://doi.org/10.2172/7115487> (United States). Center for Wave Phenomena.
- Hale, D., 1992b. Computational Aspects of Gaussian Beam Migration. Colorado School of Mines, Golden, CO (United States). <https://doi.org/10.2172/7200248>. Center for Wave Phenomena.
- Halliwel, N.A., 1991. Geometrical optics of inhomogeneous media. *J. Sound Vib.* 149, 531–532. [https://doi.org/10.1016/0022-460X\(91\)90460-2](https://doi.org/10.1016/0022-460X(91)90460-2).
- Hargreaves, N.D., Calvert, A.J., 1991. Inverse Q filtering by Fourier transform. *Geophysics* 56, 519–527. <https://doi.org/10.1190/1.1443067>.
- Henk, Keers, Don, W., et al., 2001. Viscoacoustic crosswell imaging using asymptotic waveforms. *Geophysics*. <https://doi.org/10.1190/1.1444975>.
- Hill, Ross, N., 1990. Gaussian beam migration. *Geophysics* 55, 1416–1428. <https://doi.org/10.1190/1.1442788>.
- Hill, Ross, N., 2001. Prestack Gaussian-beam depth migration. *Geophysics* 66, 1240–1250. <https://doi.org/10.1190/1.1487071>.
- Hu, H., Liu, Y.K., Zheng, Y.C., et al., 2016. Least-squares Gaussian beam migration. *Geophysics* 81, S87–S100. <https://doi.org/10.1190/geo2015-0328.1>.
- Kaelin, B., Guitton, A., 2006. Imaging condition for reverse time migration. *SEG Tech. Progr. Expand. Abstr.* 25, 2594. <https://doi.org/10.1190/1.2370059>.
- Lee, D., Mason, I.M., Jackson, G.M., 1991. Split-step Fourier shot-record migration with deconvolution imaging. *Geophysics* 56, 1786–1793. <https://doi.org/10.1190/1.1442991>.
- Mittet, R., 2007. A simple design procedure for depth extrapolation operators that compensate for absorption and dispersion. *Geophysics* 72, S105–S112. <https://doi.org/10.1190/1.2431637>.
- Mittet, R., Sollie, R., Hokstad, K., 1995. Prestack depth migration with compensation for absorption and dispersion. *Geophysics* 60, 1485–1494. <https://doi.org/10.1190/1.1443882>.
- Mu, X.R., Huang, J.P., Wen, L., et al., 2021a. Modeling viscoacoustic wave propagation using a new spatial variable-order fractional Laplacian wave equation. *Geophysics* 86, 1–74. <https://doi.org/10.1190/geo2020-0610.1>.
- Mu, X.R., Huang, J.P., Yang, J.D., et al., 2021b. Viscoelastic Wave Propagation Simulation Using New Spatial Variable-Order Fractional Laplacians. *Bulletin of the Seismological Society of America*. <https://doi.org/10.1785/0120210099>.
- Nowack, R.L., Sen, M.K., Stoffa, P.L., 2003. Gaussian Beam Migration for Sparse Common-Shot and Common-Receiver Data. *SEG Technical Program Expanded Abstracts 2003*. Society of Exploration Geophysicists, pp. 1114–1117. <https://doi.org/10.1190/1.1817470>.
- Popov, M.M., 1982. A new method of computation of wave fields using Gaussian beams. *Wave Motion* 4, 85–97. [https://doi.org/10.1016/0165-2125\(82\)90016-6](https://doi.org/10.1016/0165-2125(82)90016-6).
- Traynir, P., Liu, J., Reilly, J.M., 2008. Amplitude and bandwidth recovery beneath gas zones using Kirchhoff prestack depth Q-migration. *SEG Tech. Progr. Expand. Abstr.* 27, 3713. <https://doi.org/10.1190/1.3059363>.
- Valenciano, A.A., Chemingui, N., Whitmore, D., et al., 2011. Wave Equation Migration with Attenuation and Anisotropy Compensation. *SEG Technical Program Expanded Abstracts 2011*. Society of Exploration Geophysicists, pp. 232–236. <https://doi.org/10.1190/1.3627674>.
- Wang, J., Zhou, H., Tian, Y.K., et al., 2012. A New Scheme for Elastic Full Waveform Inversion Based on Velocity-Stress Wave Equations in Time Domain. *SEG Technical Program Expanded Abstracts 2012*. Society of Exploration Geophysicists, pp. 1–5. <https://doi.org/10.1190/segam2012-0561.1>.
- Wang, Y.H., 2002. A stable and efficient approach of inverse Q filtering. *Geophysics*

- 67, 657–663. <https://doi.org/10.1190/1.1468627>.
- Wang, Y.H., 2006. Inverse Q-filter for seismic resolution enhancement. *Geophysics* 71, V51–V60. <https://doi.org/10.1190/1.2192912>.
- Xie, Y., Xin, K.F., Sun, J., et al., 2009. 3D Prestack Depth Migration with Compensation for Frequency Dependent Absorption and Dispersion. SEG Technical Program Expanded Abstracts 2009. Society of Exploration Geophysicists, pp. 2919–2923. <https://doi.org/10.1081/22020586.2010.12041885>.
- Xu, S.B., Yue, Y.B., Wang, S.J., 2014. Elastic Gaussian beam prestack depth migration. *Oil Geophys. Prospect.* <https://doi.org/10.13810/j.cnki.issn.1000-7210.2014.02.007>, 7+48-54+76, (in Chinese).
- Yang, J.D., Zhu, H.J., 2019. Viscoacoustic least-squares reverse-time migration using a time-domain complex-valued wave equation. *Geophysics* 84, 1–130. <https://doi.org/10.1190/geo2018-0804.1>.
- Yang, J.D., Zhu, H.J., Huang, J.P., et al., 2018. 2D isotropic elastic Gaussian-beam migration for common-shot multicomponent records. *Geophysics* 83, S127–S140. <https://doi.org/10.1190/geo2017-0078.1>.
- Yue, Y.B., 2011. Study on Gaussian Beam Migration Imaging Method for Complex Media. China University of petroleum, Doctor. <https://doi.org/10.7666/d.y1877038> (in Chinese).
- Yue, Y.B., Sava, P., Qian, Z.P., et al., 2019. Least-squares Gaussian beam migration in elastic media. *Geophysics* 84, S329–S340. <https://doi.org/10.1190/geo2018-0391.1>.
- Zhang, J., Wu, J., Li, X., 2013. Compensation for absorption and dispersion in prestack migration: an effective Q approach. *Geophysics* 78, S1–S14.
- Zhang, J.F., Wu, J.Z., Li, X.Y., 2013. Compensation for absorption and dispersion in prestack migration: an effective Q approach. *Geophysics* 78, S1–S14. <https://doi.org/10.1190/geo2012-0128.1>.
- Zhang, J.H., Wapenaar, K., 2002. Wavefield extrapolation and prestack depth migration in anelastic inhomogeneous media. *Geophys. Prospect.* 50, 629–643. <https://doi.org/10.1046/j.1365-2478.2002.00342.x>.